The University of Akron
IdeaExchange@UAkron

Chemical and Biomolecular Engineering Faculty Research | Chemical and Biomolecular Engineering Department

8-15-2005

Multiscale Modeling, Simulations, and Experiments of Coating Growth on Nanofibers. Part I. Sputtering

A. Buldum

I. Busuladzic

C. B. Clemons

L. H, Dill

K. L. Kreider

See next page for additional authors

Please take a moment to share how this work helps you through this survey. Your feedback will be important as we plan further development of our repository.
Follow this and additional works at: http://ideaexchange.uakron.edu/chemengin_ideas

Part of the Chemistry Commons

Recommended Citation

Buldum, A.; Busuladzic, I.; Clemons, C. B.; Dill, L. H,; Kreider, K. L.; Young, G. W.; Evans, Edward A.; Zhang, G.; Hariharan, S. I.; and Kiefer, W., "Multiscale Modeling, Simulations, and Experiments of Coating Growth on Nanofibers. Part I. Sputtering" (2005). *Chemical and Biomolecular Engineering Faculty Research*. 10.
http://ideaexchange.uakron.edu/chemengin_ideas/10

This Article is brought to you for free and open access by Chemical and Biomolecular Engineering Department at IdeaExchange@UAkron, the institutional repository of The University of Akron in Akron, Ohio, USA. It has been accepted for inclusion in Chemical and Biomolecular Engineering Faculty Research by an authorized administrator of IdeaExchange@UAkron. For more information, please contact mjon@uakron.edu, uapress@uakron.edu.

Authors
A. Buldum; I. Busuladzic; C. B. Clemons; L. H, Dill; K. L. Kreider; G. W. Young; Edward A. Evans; G. Zhang; S. I. Hariharan; and W. Kiefer

This article is available at IdeaExchange@UAkron: http://ideaexchange.uakron.edu/chemengin_ideas/10

HTML ABSTRACT + LINKS

Multiscale modeling, simulations, and experiments of coating growth on nanofibers. Part I. Sputtering

A. Buldum
Department of Physics, University of Akron, Akron, Ohio 44325-4001

I. Busuladzic, C. B. Clemons, L. H. Dill, K. L. Kreider, and G. W. Young[a)]
Division of Applied Mathematics, Department of Theoretical and Applied Mathematics, University of Akron, Akron, Ohio 44325-4002

E. A. Evans and G. Zhang
Department of Chemical Engineering, University of Akron, Akron, Ohio 44325-3906

S. I. Hariharan
Department of Electrical and Computer Engineering, University of Akron, Akron, Ohio 44325-3904

W. Kiefer
Department of Mechanical Engineering, University of Akron, Akron, Ohio 44325-3903

(Received 30 September 2004; accepted 1 July 2005; published online 17 August 2005)

This paper is Part I of an integrated experimental/modeling investigation of a procedure to coat nanofibers and core-clad nanostructures with thin-film materials using plasma-enhanced physical vapor deposition. In the experimental effort, electrospun polymer nanofibers are coated with aluminum under varying operating conditions to observe changes in the coating morphology. This procedure begins with the sputtering of the coating material from a target. This paper focuses on the sputtering process and transport of the sputtered material through the reactor. The interrelationships among the processing factors for the sputtering and transport are investigated from a detailed modeling approach that describes the salient physical and chemical phenomena. Solution strategies that couple continuum and atomistic models are used. At the continuum scale, the sheath region and the reactor dynamics near the target surface are described. At the atomic level, molecular-dynamics (MD) simulations are used to study the sputtering and deposition mechanisms. Ion kinetic energies and fluxes are passed from the continuum sheath model to the MD simulations. These simulations calculate sputtering and sticking probabilities that in turn are used to calculate parameters for the continuum reactor model. The reactor model determines the concentration field of the coating material. © *2005 American Institute of Physics*. [DOI: 10.1063/1.2007848]

I. INTRODUCTION

Hollow nanowires and nanoscale core/clad structures have attracted great academic and industrial interest in recent years.[1–5] Improvement in the ability to synthesize hollow nanowires of different materials has resulted in the suggestion and potential development of devices based on the properties of the hollow nanowires.[1] Possible applications for nanowires in the areas of filtration,[6] composites,[7,8] biomedicine,[9,10] and electronics[2] have been suggested. However, several limitations to the widespread synthesis and use of nanoscale structures can be identified. First, the ability to produce large quantities of hollow nanowires and core-clad structures with controlled electronic and structural properties is still undeveloped. Second, the nanoscale dimensions of these materials often lead to previously unobserved properties that need to be understood and ultimately controlled.

This work addresses some aspects of these issues through a coordinated experimental and modeling program. From the standpoint of nanostructure synthesis, we examine physical vapor deposition techniques for applying coatings to electrospun polymer nanofibers. We have successfully coated fibers with films of copper, aluminum, titanium, zirconium, and aluminum nitride by using a plasma-enhanced physical vapor deposition (PEPVD) sputtering process (see Fig. 1).[11,12]

The sputtering power supply drives a 2-in.-diameter electrode which forms the target (or source) material. The nanofibers are placed on a holder that sits 8 cm above the target. A plasma is formed when electrons emitted from the target create ions in the gas phase. Once a plasma is formed, the ions strike the target and sputter neutral species, which are then transported to the nanofibers and deposited. The ions also strike the coated nanofibers, but typically at a much lower energy. The coating growth rate depends on the rate at which atoms are supplied to the nanofiber surface, the nanofiber temperature, and the ion flux to the nanofiber. The morphology of the coating depends on the mobility of the atoms on the surface and how much time the atoms have to move around before the next atoms hit the surface. The rate at which atoms are supplied to the nanofiber depends on the rate at which atoms are sputtered from the target and how far away the nanofiber is from the target. The sputtering rate depends on the ion flux, which is determined by the power applied to the target, the pressure of the system, and the

[a)]Electronic mail: gwyoung@uakron.edu

 © 2005 American Institute of Physics

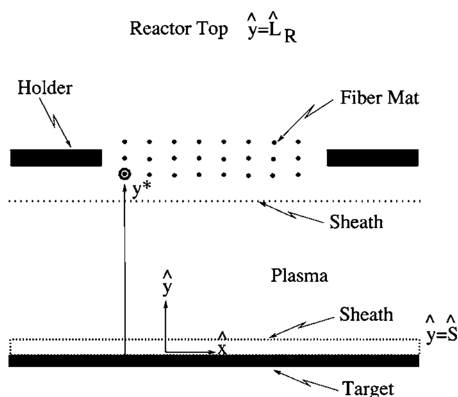

FIG. 1. Global schematic of the reactor for neutral species transport within the reactor.

working gas used. The ion flux to the nanofiber is determined by the potential drop between the plasma and the nanofiber, the working gas used, and the pressure.

Transmission electron microscopy (TEM) is used to determine the effects of these variables on the film growth rate and morphology. The average thicknesses of the fibers before and after the coating process are compared to determine an average growth rate of the films. To determine coating morphology and crystalline structure, TEM images and diffraction patterns are taken. Removing the nanofiber core leaves a polycrystalline nanotube of the coating material which verifies that the coating is continuous around the fiber.

Figure 2 shows a TEM image of an aluminum-coated fiber. The cylindrical cross-section of a tube is shown in Fig. 3, which indicates that the tube did not collapse after the polymer inside was removed. The smallest inner diameter of the tubes is around 20 nm. The approximate thickness of the wall of the tubes was controlled by the sputtering process. A tube with different wall thickness is shown in Fig. 4.

The approach described above can be used to produce

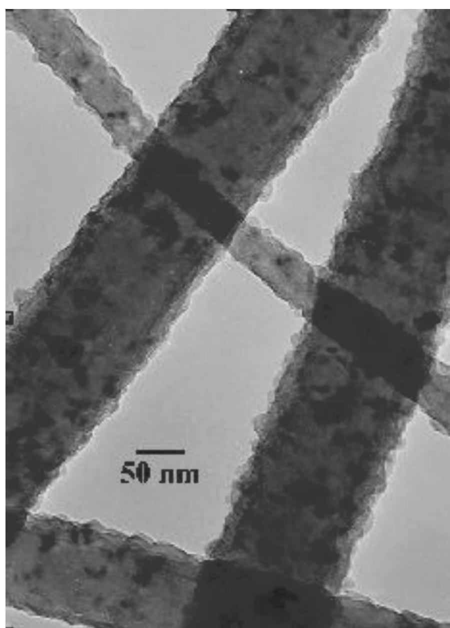

FIG. 2. TEM images of aluminum-coated fibers.

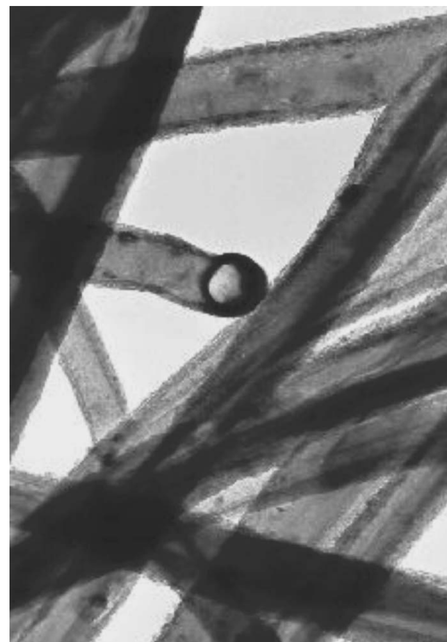

FIG. 3. TEM image of an aluminum nanotube.

cylindrical, multilayered nanostructures with precisely controlled interfaces composed of many materials, including metals, semiconductors, ceramics, and polymers with controlled diameters and a range of nanometer thickness walls.

II. OVERALL MODELING APPROACH

The model for the coating of nanofibers is based upon deposition within a traditional PEPVD system. The objective is to determine the influence of process conditions on the uniformity and morphology of the coating. The system is characterized by a bulk gas phase dominated by neutral species, and sheath regions that separate the bulk gas phase from the substrate (nanofibers) and the target, as shown in Fig. 1. There are several disparate geometrical length scales in the reactor system. The reactor size from target to the top is not more than 20 cm, in length. The distance from the target to

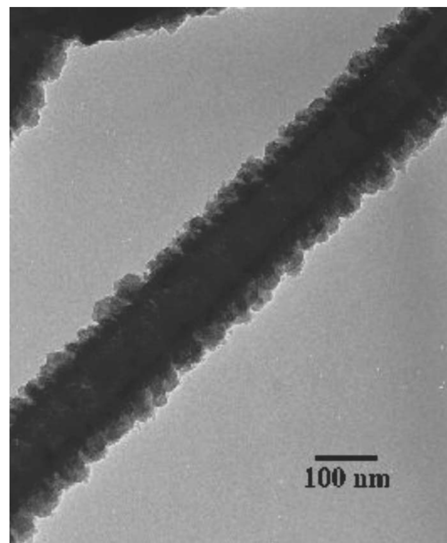

FIG. 4. Aluminum nanotube of wall thickness of 40 nm.

the holder is centimeters in length. The sheath thicknesses are on the order of millimeters. The nanofibers are, on average, 100 nm in diameter. Furthermore, the nanofiber mat is a sparse mesh of the fibers. Hence, the assumption is made that the holder region of nanofibers does not influence the global transport of neutral species within the reactor. Thus, the overall transport of neutral species is separated into two components. The present paper examines the global component model for the sputtering and transport of sputtered atoms away from the target, as shown in Fig. 1, without any influence from the sparse mesh of nanofibers and the holder. The local component models the neutral species transport in the vicinity of a nanofiber. This is the topic of Part II of this series of papers.[13] The global information for neutral species concentration at a nanofiber location, $y=y^*$, serves as the far-field input to the local model of deposition on the nanofiber.

The modeling must also include ions that accelerate to the substrate and sputter material from the deposited coating. This material re-emits into the plasma. Hence, the coating process is complicated by the sensitivity to both the reactor scale process variables and the surface topography of the coating. This feedback deals with different length scales, spanning tens of centimeters at the reactor scale to nanometers at the surface feature scale of the coating. These factors indicate a strong need for an integrated approach in the simulation process, in which both the reactor properties and the details of the topography are taken into account. The reactor level process variables influence the surface feature coating profile, while the coating feature processes can affect the entire reactor level characteristics as feature scale information is introduced to the global level. Simulation of this feedback between surface features and the reactor level is difficult to accomplish, given current computational abilities. Thus, efficient solution methodologies integrating simulations at the various length scales must be developed.[14–17] This paper together with Ref. 13 present a strategy for accomplishing this integration through the linking of models at the global reactor scale, the local nanofiber scale, and the molecular scale.

For the remainder of this paper, consider the target region and transport of the deposition material by diffusion for the global reactor system. The Poisson and ion fluid equations govern the transport of ions through the sheath region, and the interaction of the ions with the target. Mass balance equations at the target include deposition rate parameters and desorption parameters due to ion bombardment. These parameters are functions of the ion flux to the surface and the ion kinetic energy. These parameters are passed to the continuum equations from molecular-dynamics simulations that are described below.

III. NEUTRAL SPECIES TRANSPORT MODEL

A. Formulation

A variety of analytical and computational modeling approaches have been applied to describe sputtering and transport of sputtered material through the target-substrate drift space.[18–22] In these models, sputtered material leaves the target with momentum due to the action of the ions chipping away the target material. This ballistic transport occurs over a zone of thermalization, the length of which decreases with pressure. Outside this zone, diffusion quickly becomes the mechanism which carries the sputtered material through the plasma region. Due to the larger pressures and the relatively large (compared to the mean free path) distance from the target to the holder in our system, the ballistic component is neglected and purely diffusive transport is assumed. This assumption is further justified by considering the value of the Knudsen number K_n for our system. The Knudsen number, which is the ratio of the mean free path to a characteristic length scale of the system, gives a rough indication of the flow regime in the system. A Knudsen number much less than one implies a fluid flow or viscous flow, while K_n much greater than one implies a molecular flow regime. In our system, under typical operating conditions, K_n is in an intermediate regime with values ranging from 0.03 to 0.1 depending on the characteristic length chosen and the method used for calculating the mean free path.

For simplicity, assume that the global transport problem is one-dimensional, as shown in Fig. 1. This assumption is reasonable since the holder region is small in comparison to the size of the reactor, so the sidewall effects can be ignored. Also assume that the temperature in the reactor is constant for this formulation (energy transport can be included in the model if necessary). Inside the reactor and outside of the sheath region, assume that the concentration $\hat{C}$ of deposition material (neutral molecules) is large compared to the ion concentration, and that the mode of transport of the deposition material is primarily governed by diffusion,

$$\hat{C}_{\hat{t}} = \hat{D}\hat{C}_{\hat{y}\hat{y}}, \tag{1}$$

where $\hat{D}$ is the mass diffusivity. At the top of the reactor, $\hat{y} = \hat{L}_R$, assume a no flux condition,

$$\hat{C}_{\hat{y}} = 0. \tag{2}$$

The source of concentration at the target surface, $\hat{y}=0$, is governed by

$$\hat{D}\hat{C}_{\hat{y}} = k(\hat{J},\hat{\epsilon})\hat{C} - k_{\text{ions}}(\hat{J},\hat{\epsilon}), \tag{3}$$

where k is the reaction coefficient for sputtered material that readsorbs to the target surface and k_{ions} is the desorption rate from sputtering due to ion bombardment of the target surface. These rate coefficients depend on $\hat{J}$, the ion flux to the surface and $\hat{\epsilon}$, the ion kinetic energy. In the solution procedure below, these two quantities are obtained by examining the sheath region around the target. Once determined, these quantities are passed to a molecular-dynamics (MD) simulation to determine k and k_{ions}. Knowing these parameters, the concentration $\hat{C}$ is then determined in the reactor. This concentration field serves as the input for the local transport model discussed in Ref. 13. Hence, the main thrust of this work is to use a coupled continuum/atomistic approach to find expressions for k and k_{ions}. Note also that the units of concentration are mole/volume, the units of k are length/time, and the units of k_{ions} are mole/(area × time).

The governing equations and boundary conditions are nondimensionalized using the following scalings:

Dimensional variable	Scale
$\hat{y}$	$\hat{L}_R$
$\hat{C}$	C^*
$\hat{t}$	$\hat{L}_R^2/\hat{D}$

Note that C^*, the reference global reactor concentration, is specified in (8) below. These scalings lead to the nondimensional groups,

$$D_k = \frac{k\hat{L}_R}{\hat{D}} = \frac{\text{rate of reactions at the target}}{\text{rate of transport by diffusion}},$$

$$D_{k_{\text{ions}}} = \frac{k_{\text{ions}}\hat{L}_R}{\hat{D}C^*} = \frac{\text{rate of sputter at the target}}{\text{rate of transport by diffusion}}.$$

The nondimensional governing equation is

$$C_t = C_{yy}. \tag{4}$$

The boundary condition at $\hat{y}=\hat{L}_R(y=1)$ becomes

$$C_y = 0, \tag{5}$$

and the boundary condition at $\hat{y}=0(y=0)$ is

$$C_y = D_k C - D_{k_{\text{ions}}}. \tag{6}$$

B. Solution

As stated above, the ballistic transport of sputtered neutral species can be neglected and purely diffusive transport can be assumed. Moreover, the concentration of the sputtered material quickly reaches steady state at the global scale.

Hence, the steady-state solution to Eq. (4) is a constant,

$$C = \frac{k_{\text{ions}}}{kC^*}, \tag{7}$$

where the values of k_{ions} and k are to be determined by MD calculations. It is then convenient to specify the reference concentration C^* as

$$C^* = \frac{k_{\text{ions}}}{k}. \tag{8}$$

IV. THE SHEATH MODEL NEAR THE TARGET

A. Formulation

The intent of the modeling is to connect macroscale phenomena to nanoscale phenomena by linking simple models at each length scale. Hence, in the sheath region near the target we seek a model to reasonably approximate the physics. In the experiments we use an rf sputtering head. We approximate the plasma as a uniform cylindrical column in an intermediate pressure regime [mean free path less than or equal to the characteristic lengths of the plasma but greater than the ratio of ion temperature to electron temperature multiplied by the characteristic length of the plasma (Lieberman and Lichtenberg[23])]. Under these conditions it is reasonable to assume that the voltage drop occurs almost entirely across the sheath region.

In the experiments, which will provide a basis for comparison in Paper III of the series, a 2-in. aluminum target is sputtered in a background gas of argon. The pressure is varied between 4 and 40 mtorr, the power is varied between 50 and 150 watts, and the target to substrate distance is 8 cm. No external bias is applied to the target or substrate (the substrate is grounded). We estimate, based on a uniform plasma model,[23] that the voltage difference between the target and the plasma is 500 V and the voltage difference between the holder and the plasma is 10 V (see Fig. 1). We expect that there is a voltage field within the bulk plasma but that the variation in voltage across the bulk plasma is very small relative to the voltage change across the sheaths. Hence, we isolate the sheath models from each other even though their potential drops are not independent. Our operating conditions are near the edge of consistency with the assumptions of a uniform plasma model approximation (Lieberman and Lichtenberg[23]) and with the time-averaged model of Economou *et al.*[24] The latter is the basis for the sheath model at the target.

The plasma ionizes a small fraction of the background gas and the potential across the sheath region accelerates these ions toward the target. Upon impact, the target material is ejected or sputtered into the plasma. The rate of sputtering is related to the kinetic energy and flux of the bombarding ions. In this section, a sheath model is developed to relate the applied power, pressure, and temperature to the kinetic energy and flux at the target.

The sheath layer, typically only a few millimeters in thickness, is thin relative to the size of the reactor. By ignoring end effects, the sheath is modeled as a one-dimensional region that possesses a positive space charge due to an overabundance of positively charged ions. Temperature gradients and magnetic fields in the region are ignored. Assume the ions satisfy the continuity equation,

$$\frac{d}{d\hat{y}}(\hat{u}\hat{n}) = 0, \tag{9}$$

in which $\hat{u}(\hat{y})$ is the velocity of the ions and $\hat{n}(\hat{y})$ is their number density. The coordinate $\hat{y}$ represents distance from the target, as shown in Fig. 1. Ions conserve momentum according to the equation

$$\hat{u}\frac{d\hat{u}}{d\hat{y}} = -\frac{q\hat{E}}{m} + \frac{\alpha\hat{u}^2}{m}, \tag{10}$$

where q and m are the charge and mass, respectively, associated with a single ion, and $\hat{E}$ is the local electric field. The first two terms in (10) represent inertia and electromotive force, respectively. The last term represents the effect of ions colliding with the background nonionized gas atoms or molecules, and α represents the strength of this interaction. The gradient of the electric field is related to the charge density according to the equation

$$\frac{d\hat{E}}{d\hat{y}} = -\frac{q\hat{n}}{\varepsilon_0}. \tag{11}$$

Here, ε_0 is the vacuum permittivity. The final field equation relates the electric field to the electrical potential,

$$\hat{E} = \frac{d\hat{V}}{d\hat{y}}. \tag{12}$$

The Bohm criterion and quasineutrality[24,25] are used to define boundary conditions for this system of first-order differential equations. We refer the reader to Ref. 24 for a thorough discussion of the boundary conditions. Ordinarily this system would require four boundary conditions. However, the location $\hat{y}=\hat{S}$ at which the sheath layer ends is also an unknown and must be determined as part of the solution, so a fifth boundary condition is needed. Four boundary conditions are applied at $\hat{y}=\hat{S}$,

$$\hat{n}(\hat{S}) = \hat{n}_p, \tag{13}$$

$$\hat{u}(\hat{S}) = -\sqrt{\frac{k_B T_e}{m + 2\alpha\lambda_D}}, \tag{14}$$

$$\hat{E}(\hat{S}) = \frac{k_B T_e}{2q\lambda_D}, \tag{15}$$

and

$$\hat{V}(\hat{S}) = \hat{V}_a, \tag{16}$$

and one at the target surface,

$$\hat{V}(0) = 0. \tag{17}$$

In these expressions, $\hat{n}_p$ is the ion number density in the plasma, $k_B = 1.38\times 10^{-23}$ J/K is the Boltzmann constant, T_e is the electron temperature (in Kelvin), and λ_D is the Debye length,

$$\lambda_D = \sqrt{\frac{\varepsilon_0 k_B T_e}{\hat{n}_p q^2}}. \tag{18}$$

The constant $\hat{V}_a$ that appears in (16) is the applied voltage. This voltage drop and the plasma ion density $\hat{n}_p$ are both assumed controllable and therefore specified by the operator. In particular, the voltage drop between the plasma and the target, and the plasma density depend on the applied power, the pressure, and the characteristic length scales (radius and length) of the plasma column.[23] Roughly, the voltage increases as the square root of the applied power at high power, and increases linearly with pressure over the pressure range of interest in this work (0.01–0.05 torr); at higher pressures the voltage drop does not change significantly with increasing pressure. The plasma ion density (and the electron density) depends most sensitively on the pressure, increasing as the square of the pressure, but also increasing linearly with power. Therefore, all constants that appear within this system of equations are either material properties or can be experimentally controlled, at least in principle.

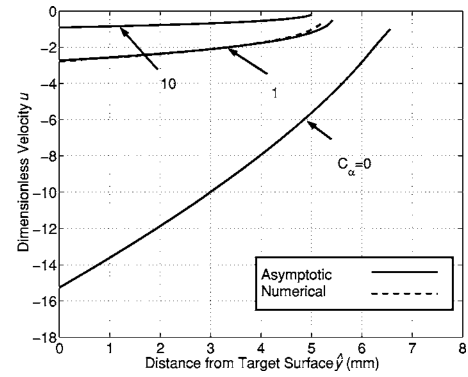

FIG. 5. Dimensionless ion velocities as a function of distance from the target surface for several values of C_α with $\hat{V}_a=100$ V and $T_e=10^4$ K.

The solution of the sheath model for the ion velocity is presented in the Appendix. Using the ion velocity we determine the ion flux and kinetic energy.

B. Results

The controllable operating conditions for the reactor are pressure, power, temperature, target-nanofiber distance, mat porosity, and initial nanofiber radius. These parameters and ranges of their values will be more thoroughly discussed in Part III of this series. Representative values are used in the results that follow. Furthermore, the voltage drop between the plasma and the target, the plasma density, and the electron temperature depend on the applied power, the pressure, and the characteristic length scales (radius and length) of the plasma column. These dependencies will also be more thoroughly discussed in Part III of this series. Representative ranges of these values are used in the results that follow.

Dimensionless ion velocities u are plotted against distance $\hat{y}$ from the target in Fig. 5 for three values of the collision parameter: $C_\alpha=0$, 1, and 10 [see the Appendix for asymptotic and numerical solution details, and for the definition of $C_\alpha=(\alpha\lambda_D)/m$]. The assumed applied voltage across the sheath is $\hat{V}_a=100$ V and the temperature is $T_e=10^4$ K. The ion density $\hat{n}_p$ in the plasma is taken as approximately 10^{15} atoms/m^3, the vacuum permittivity ε_0 of the sheath region is 8.9×10^{-12} F/m, and the charge q of the species is 1.6×10^{-19} C. The solid and dashed curves in the figure represent asymptotic and numerical results, respectively. Asymptotic and numerical results coincide for $C_\alpha=0$ and 10. The difference observed for $C_\alpha=1/\varepsilon=1$ may be attributed to the error in the asymptotic solution, which assumes $\varepsilon \ll 1$, a condition that is clearly violated in this case. Similar results are obtained for applied voltages $\hat{V}_a=10$ V and $\hat{V}_a=500$ V and for electron temperatures up to $T_e=2.6\times 10^4$ K, which represent ranges of current interest. These results suggest that the numerical solution for the ion velocity is fully reliable.

The figure also shows the sensitivity of the ion velocity to the parameter C_α: the scale of $|u|$ increases by an order of magnitude as C_α decreases from unity to zero. The sheath thickness $\hat{S}$ simultaneously increases modestly from approxi-

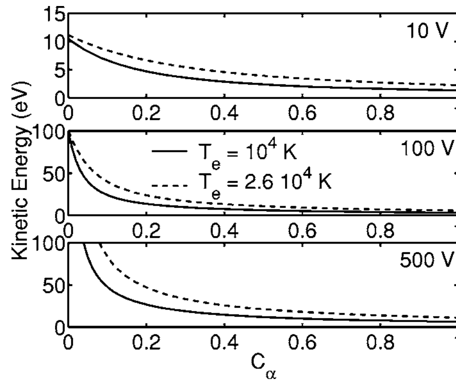

FIG. 6. Kinetic energy as a function of collision parameter.

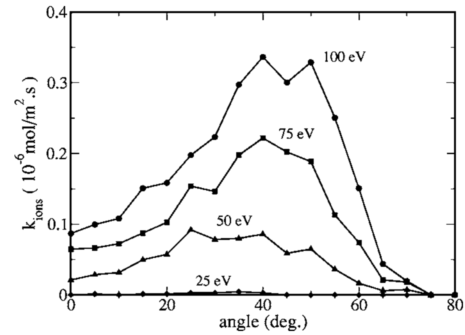

FIG. 7. Values of k_{ions} as a function of incident angle for incoming argon ions with various kinetic energies.

mately 5.3 to 6.6 mm. The sheath thickness corresponds to the positive distance from the target where a curve in the figure terminates.

Figure 6 shows the kinetic energy $(m\hat{u}^2/2)$ with which ions impact the target as a function of the collision parameter C_α for three different voltages across the sheath, $\hat{V}_a=10$, 100, and 500 V, and two different electron temperatures, $T_e=10^4$ and 2.6×10^4 K. Expressed as potentials $(k_B T_e/q)$, these electron temperatures are 0.863 and 2.24 V, respectively. As for the selected voltage range, it is believed that the applied voltage across the sheath layer is on the order of 100 V based on a uniform plasma model for these conditions.[23] To see the effect of voltage on the kinetic energy, we also consider one order of magnitude less and one more. A kinetic energy of 50 eV or more is believed necessary for target material to be sputtered into the plasma.

In the top graph in Fig. 6, it is seen that the applied voltage, $\hat{V}_a=10$ V, is too low for sputtering to occur for all temperatures considered and all values of the collision parameter. The middle graph shows that when the applied voltage is $\hat{V}_a=100$ V, kinetic energies of 50 eV are achieved provided the collision parameter is less than 0.1. At the highest applied voltage $\hat{V}_a=500$ V, this kinetic-energy threshold is achieved for a collision parameter of 0.2 at the highest temperature. The collision parameter must be less than 0.1 at the lower temperature to achieve the given threshold.

V. CALCULATION OF SPUTTERING AND STICKING PROBABILITIES AND RATE COEFFICIENTS BY MOLECULAR-DYNAMICS SIMULATION

The solution (7) of the global diffusion problem requires the values of two coefficients, the readsorption rate k and the desorption rate k_{ions}, which first appear in boundary condition (3). These coefficients are computed using molecular-dynamics simulations at the atomic scale. The MD simulations consist of an atomic model of the system where the initial positions of atoms or molecules and the interactions between the atoms or molecules are specified. Classical equations of motion (Newton's) are solved numerically.[26] Previously, MD simulations have been very useful for the investigation of metallic film growth by physical vapor deposition.[16,27–30] Such simulations provide the probabilities of adsorption, reflection, and sputtering events due to an incoming particle by tracking the trajectories of individual atoms.

In order to run the MD simulation, the velocity, kinetic energy, and flux of the bombarding particles are specified as described in Sec. IV. The bombarding particles can be argon ions or aluminum atoms. The same simulation can be used for either particle because both have roughly the same mass.[31] The only difference is in the kinetic energy—it is assumed that the kinetic energy of an incoming argon ion is much greater than that of an aluminum atom that approaches the target through diffusion.

The MD simulations were run with 275 particles bombarding a flat aluminum target. The target consists of twelve Al(111) layers (hence 3840 atoms) and the bottom two layers of the target are taken to be robust. The interaction between Al atoms is modeled by an extensively tested embedded atom-type (or glue type) potential[32] with a repulsive potential[28] for the short-range interaction of Al atoms with kinetic energies above 10 eV. The target is thermalized at the reactor temperature, 500 K, and the time step is taken as $\Delta t=1.0$ fs. The kinetic energies of the incoming argon ions are specified to be 25, 50, 75, and 100 eV. These values are in the range suggested by the sheath model. Incident angles of 0°–80° from the normal with a 5° increment were used in order to determine the angular dependence of k and k_{ions}. A single run (275 particles at one kinetic energy at one incident angle) takes about 24 h to complete on an INTEL-based workstation.

In order to obtain the desorption rate k_{ions} for a fixed incident angle, the 275 bombarding particles are sent in one at a time and the number of aluminum atoms sputtered off the surface is counted. The ratio of this number to 275 (the number of incoming argon ions) is computed. This ratio is multiplied by the flux $\hat{n}\cdot\hat{u}$ from the target sheath model and divided by Avogadro's number to get k_{ions}. The experiment is repeated with different incident angles to obtain the angular dependence of k_{ions}.

Figure 7 shows the values of k_{ions} as a function of incident angle for incoming argon ions with kinetic energies of 25, 50, 75, and 100 eV, which are consistent with the sheath model. As expected, k_{ions} increases with kinetic energy. Furthermore, k_{ions} tends to achieve a maximum value for incident angles around 45°.

In order to obtain the readsorption rate k for a fixed

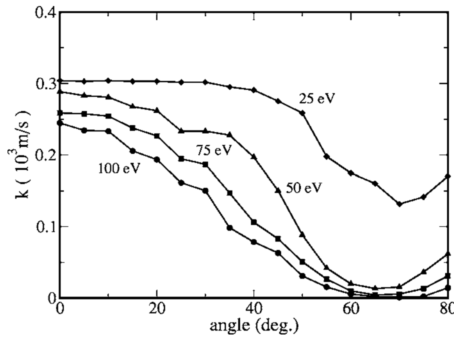

FIG. 8. Values of k as a function of incident angle for incoming aluminum atoms with various kinetic energies.

incident angle, the incoming particles are now considered to be aluminum atoms that hit the target via diffusion. The 275 bombarding particles are sent in one at a time and the number of aluminum atoms that are sputtered and then reattached is counted. The ratio of this number to 275 (the number of incoming aluminum atoms) is computed. This ratio is multiplied by the velocity of the sputtered aluminum atoms to determine k. This velocity is estimated using the expression $\sqrt{k_B T / m_{Al}}$, where m_{Al} is the mass of an aluminum atom. For this calculation it is also assumed that the sputtered atoms eventually equilibrate at $T=300$ K.

Figure 8 shows the values of k as a function of incident angle for incoming aluminum atoms with kinetic energies of 25, 50, 75, and 100 eV. It is seen that k decreases with kinetic energy, since highly energetic atoms do not easily readsorb onto the target. Furthermore, atoms that strike the target with normal incidence are more likely to readsorb.

Figure 9 shows the values of k and k_{ions} as a function of the kinetic energy of the incoming particles for normal incidence, consistent with the one-dimensional continuum model. These are the values used to obtain the aluminum concentration in the plasma, presented in (7) and (8). In Fig. 9 it is seen that k decreases nearly linearly with kinetic energy, whereas k_{ions} increases nearly linearly for the kinetic energies of interest. Furthermore, there is no sputtering for incoming kinetic energies below 25 eV.

We note that if the mean free path of the ion-neutral

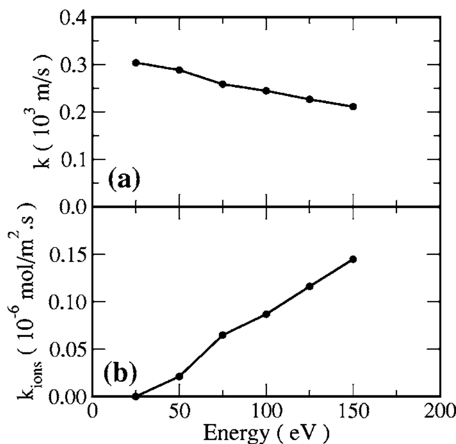

FIG. 9. Values of k and k_{ions} as a function of the kinetic energy of the incoming particles for normal incidence.

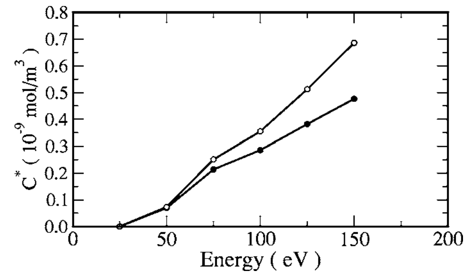

FIG. 10. C^* as a function of the kinetic energy of incoming particles.

collisions is comparable with the sheath length (which should be the case in the present experiment), the ion energy distributions at the target becomes rather broad, ranging from 0 to some maximum energy. In order to calculate this ion energy distribution accurately, a fully kinetic approach is necessary. In our simple fluid model to describe the sheath physics, the kinetic effects are neglected. Hence, for the purposes of this paper we are making the assumption that the energy distribution of the ions has been averaged and can be approximated as monoenergetic in order to get a simple solution. This is partly justified through our MD simulations, which show that the etched atoms appear to have similar energies (in the range of 1–10 eV for normal incident angles) over a broad range of bombarding ion energies. Similar results were found in the MD simulations of Refs. 33 and 34. We are most interested in these etched atoms since this species is being deposited onto the nanofibers. Future versions of the model will include an analysis of the effect of the ion energy distribution on the resulting deposition. In particular, the ion energy distribution may affect the concentration of deposition material. The second paper of this series demonstrates that the value of this concentration affects the deposition rate at the nanofibers.

VI. REACTOR MODEL RESULTS

Figure 10 shows the value of the concentration $C^* = k_{ions}/k$, as defined by (8), as a function of kinetic energy of the incoming particles. The two lines in this figure are determined as follows. The upper line is calculated as the ratio of Fig. 9(b) to Fig. 9(a) for the same kinetic energy of bombarding argon ions and incoming aluminum atoms. The lower line assumes a perfect readsorption so that k is calculated using a sticking probability of one. This assumption maximizes the value of k which leads to a decrease in the value of C^*. Given the uncertainty of the kinetic energies of the aluminum atoms, the two lines thus represent lower and upper limits for the values of C^*. Note that the calculated values of C^* lead to the number density values of C^* that are similar in magnitude to the size of the ion density $\hat{n}_p$.

VII. SUMMARY

Polymer nanofibers are produced by electrospinning, and then coated using rf magnetron sputtering. The resulting composite structure is then heated to remove the polymer core, leaving a nanotube. We develop a comprehensive model integrated across atomic to continuum length scales for simulating the sputtering and transport of coating mate-

rial in this coating process. In this paper, the interrelationships among processing factors for the sputtering and transport are investigated from a detailed modeling approach that describes the salient physical and chemical phenomena. Solution strategies that couple continuum and atomistic models are used. Information is passed between the various length scale models so that the simulations are integrated together. To keep the numerical simulations at a manageable level, asymptotic analyses are used to reduce the complex models to simpler, but still relevant, models. Furthermore, the asymptotic solutions are used to verify the full numerical simulations in limiting cases.

At the continuum scale, we describe the sheath region and the reactor dynamics near the target surface. At the atomic level, we use molecular-dynamics (MD) simulations to study the sputtering and deposition mechanisms. Ion kinetic energies and fluxes are passed from the continuum sheath model to the MD simulations. These simulations calculate sputtering and sticking probabilities that in turn are used to calculate parameters for the continuum reactor model. The reactor model determines the concentration field of the coating material. This field serves as the input to the deposition problem (Part II of the series) considered in Ref. 13. To prove applicability of the results, we must benchmark the model against the experimental data as processing parameters are varied. This benchmarking is the subject of Part III of this series.

ACKNOWLEDGMENTS

This work was supported by NSF Grant Nos. DMS 03-05580 and DMI-0403835, and NASA Grant Nos. NCC3-1094 and NNC04GB27G. We thank the referees for their many helpful comments and for providing a discussion on the kinetic effects for the ion energy distribution at the target.

APPENDIX: SOLUTION

The system of equations (9)–(17) is nondimensionalized with the selection of the following scales for length, number density, velocity, electric field, and potential, respectively: λ_D, $\hat{n}_p$, $\sqrt{k_BT_e/m}$, $k_BT_e/q\lambda_D$, and k_BT_e/q. Dimensionless variables below are hatless versions of their dimensional counterparts. The following dimensionless field equations are obtained:

$$(un)' = 0, \tag{A1}$$

$$\tfrac{1}{2}(u^2)' = -V' + C_\alpha u^2, \tag{A2}$$

$$V'' = -n. \tag{A3}$$

Note that the electric-field equation is eliminated in favor of the potential function, and that primes denote differentiation with respect to y. The dimensionless constant

$$C_\alpha = \frac{\alpha\lambda_D}{m} \tag{A4}$$

represents the effect of collisions in slowing the ions. The boundary conditions imposed at $S=\hat{S}/\lambda_D$ are

$$n(S) = 1, \tag{A5}$$

$$u(S) = -\frac{1}{\sqrt{1+2C_\alpha}}, \tag{A6}$$

$$V(S) = V_a, \tag{A7}$$

and

$$V'(S) = \tfrac{1}{2}. \tag{A8}$$

Lastly, the potential function is zero on the target itself,

$$V(0) = 0. \tag{A9}$$

The constant

$$V_a = \hat{V}_a/(k_BT_e/q)$$

is the dimensionless applied voltage at the sheath edge.

Integrate (A1) and apply boundary conditions (A5) and (A6) to find the relation

$$n = J(u^2)^{-1/2}. \tag{A10}$$

Here, J is interpreted as the ion flux directed toward the target, and is given by the positive constant

$$J = |u(S)| = \frac{1}{\sqrt{1+2C_\alpha}}. \tag{A11}$$

Note that the dimensional flux, $\hat{J}=|\hat{n}\hat{u}|$, of ions impacting the surface is given by $\hat{J}=\hat{n}_p\sqrt{k_BT_e/(m+2\alpha\lambda_D)}$.

Next, differentiate (A2) and use (A3) and (A10) to eliminate the potential. This operation yields the following governing equation for the velocity:

$$\tfrac{1}{2}(u^2)'' = J(u^2)^{-1/2} + C_\alpha(u^2)'. \tag{A12}$$

The velocity satisfies two conditions at $y=S$:

$$u(S) = -J \tag{A13}$$

and

$$u'(S) = \frac{J}{2}. \tag{A14}$$

The latter condition follows from (A2) and (A8).

The general methodology is now easily seen. The system (A1)–(A9) has been reduced to a single nonlinear boundary value problem (A12)–(A14). However, both the sheath edge $y=S$ and the velocity $u(y)$ are unknown and must be determined together. The approach uses the following expression for the potential function as the starting point:

$$V(y) = C_\alpha\int_0^y u^2 dy - \frac{u^2(y) - u^2(0)}{2}. \tag{A15}$$

This expression is obtained by integrating the momentum equation (A2) and using boundary condition (A9). An expression for $u(y)$ is determined, either numerically or asymptotically, by assuming a value for S and solving (A12)–(A14). Then the value of S is adjusted by a standard root-finding algorithm such as the secant method to find the root of $f(S)=V(S)-V_a$, so that boundary condition (A7) is

satisfied. When the proper value of S has been found, the solution of (A12)–(A14) also gives the correct velocity $u(y)$.

The focus now turns toward integrating Eq. (A12), a nonlinear second-order ordinary differential equation, for the velocity. An exact solution for all values of the single parameter C_α is not feasible. However, the equation can be solved for the two asymptotic limits of $C_\alpha \ll 1$ and $C_\alpha \gg 1$. For intermediate values of C_α, Mathematica's NDSOLVE function (version 4) was used to generate numerical solutions. The two asymptotic solutions are derived below.

First consider the case of a collision-free sheath region ($C_\alpha=0$ and $J=1$). Equation (A12) becomes

$$\tfrac{1}{2}(u^2)'' = (u^2)^{-1/2}, \tag{A16}$$

and the boundary conditions become

$$u(S) = -1 \text{ and } u'(S) = \tfrac{1}{2}. \tag{A17}$$

Multiply the differential equation by $(u^2)'$, integrate twice, use the boundary conditions to eliminate the constants of integration, and obtain the cubic equation

$$u^3 + a_1 u^2 + a_3 = 0,$$

with $a_1=-21/8$ and

$$a_3 = 4\left(\frac{7}{8}\right)^3 + \frac{9}{2}\left(S - y + \frac{11}{24}\right)^2.$$

The discriminant of the cubic equation, which reduces to

$$\frac{a_3}{4}\left[a_3 - 4\left(\frac{7}{8}\right)^3\right],$$

is positive. Therefore only one real solution of the cubic equation exists. The solution is given by

$$u(y) = -\tfrac{1}{8}[49\Psi(y)^{-1/3} - 7 + \Psi(y)^{1/3}], \tag{A18}$$

with

$$\Psi(y) = 343 + 16\Phi^2(y) - 4\sqrt{2}\Phi(y)\sqrt{343 + 8\Phi^2(y)}, \tag{A19}$$

and

$$\Phi(y) = 6\sqrt{2}(S-y) + \frac{11\sqrt{2}}{4}. \tag{A20}$$

For the asymptotic limit of high resistance to ion motion, $C_\alpha \gg 1$, let $\varepsilon = 1/C_\alpha$. In this regime, the electromotive driving force and the collision force opposing ion motion are of the same order of magnitude. This in turn leads to the conclusion that the velocity scale is $O(\sqrt{\varepsilon})$. Set

$$u = -\sqrt{\varepsilon w}, \tag{A21}$$

and

$$j = J/\sqrt{\varepsilon} = (2+\varepsilon)^{-1/2}, \tag{A22}$$

to obtain the governing equation

$$\frac{\varepsilon w''}{2} = j w^{-1/2} + w'. \tag{A23}$$

The small parameter ε multiplies the highest derivative, which suggests the presence of a boundary layer. Therefore the initial term of the above expression should be retained. Boundary conditions satisfied by w are

$$w(S) = j^2 \text{ and } w'(S) = -j^2. \tag{A24}$$

Assume a solution of the form $w=w_0+\varepsilon w_1+\cdots$ and obtain the following problem at leading order:

$$w_0' + \frac{1}{\sqrt{2}} w_0^{-1/2} = 0, \qquad w_0(S) = \tfrac{1}{2} \text{ and } w_0'(S) = -\tfrac{1}{2}. \tag{A25}$$

Observe that both conditions cannot be satisfied, so a boundary layer at $y=S$ is expected with w representing the outer solution. Integration of the differential equation gives the leading-order outer solution

$$w_0(y) = \left(a - \frac{3y}{2\sqrt{2}}\right)^{2/3}, \tag{A26}$$

in which the constant a is obtained via matching between the inner and outer solutions. To match the two conditions, it is also necessary to solve the w_1 outer problem,

$$w_1' - \frac{1}{(2w_0)^{3/2}} w_1 = \frac{1}{2} w_0'' + \frac{1}{4\sqrt{2w_0}}. \tag{A27}$$

The general solution of this problem may be expressed as

$$w_1(y) = \frac{4\sqrt{2}b + y + \ln w_0(y)}{4\sqrt{2w_0(y)}}, \tag{A28}$$

in which b is a second constant of integration.

To investigate the boundary layer, define the inner variable

$$\eta = (S-y)/\varepsilon, \tag{A29}$$

and set $w(y)=W(\eta)$. The inner problem then becomes

$$W_{\eta\eta} = 2\varepsilon j W^{-1/2} - 2W_\eta, \qquad W(0) = j^2 \text{ and } W_\eta(0) = \varepsilon j^2, \tag{A30}$$

in which the subscripts denote differentiation with respect to the inner variable. Setting $W=W_0+\varepsilon W_1+\cdots$, we find the leading-order inner problem,

$$W_{0\eta\eta} + 2W_{0\eta} = 0, \qquad W_0(0) = 1/2 \text{ and } W_{0\eta}(0) = 0, \tag{A31}$$

which has the solution $W_0(\eta)=1/2$. The first-order inner problem,

$$W_{1\eta\eta} + 2W_{1\eta} = 2, \qquad W_1(0) = -1/4 \text{ and } W_{1\eta}(0) = 1/2, \tag{A32}$$

has the solution $W_1(\eta)=\frac{1}{4}e^{(-2\eta)}+\eta-1/2$.

Application of the usual matching requirement at leading order gives $a=(3S+1)/2\sqrt{2}$, and at first order $b=(\ln 2 - S - 2)/4\sqrt{2}$. The composite solution $w_{\text{comp}}=(\text{inner})+(\text{outer})-(\text{common part})$ is given by

$$w_{\mathrm{comp}}(y) = w_0(y) + \varepsilon w_1(y) + \frac{\varepsilon}{4}\exp[-2(S-y)/\varepsilon], \quad (A33)$$

with the leading- and first-order contributions to the outer field now given by

$$w_0(y) = \tfrac{1}{2}[1 + 3(S-y)]^{2/3},$$
$$w_1(y) = \frac{2\ln[1+3(S-y)] - 6 - 3(S-y)}{12[1+3(S-y)]^{1/3}}. \quad (A34)$$

The ion velocity for $\varepsilon = 1/C_\alpha \ll 1$ is then given by

$$u(y) = -\sqrt{\varepsilon w_{\mathrm{comp}}(y)}. \quad (A35)$$

[1]P. G. Collins and P. Avouris, Sci. Am. (Int. Ed.) **283**, 62 (2000).
[2]Y. Cui and C. M. Lieber, Science **291**, 851 (2001).
[3]X. Duan, Y. Huang, J. Wang, and C. M. Lieber, Nature (London) **409**, 66 (2001).
[4]Y. Zhang, T. Ichihashi, E. Landree, F. Nihey, and S. Iijima, Science **285**, 1719 (1999).
[5]Y. Zhang, K. Suenaga, C. Colliex, and S. Iijima, Science **281**, 973 (1998).
[6]A. Buer, S. C. Ugbolue, and S. B. Warner, Text. Res. J. **71**, 323 (2001).
[7]P. W. Gibson, H. L. Schreuder-Gibson, and D. Rivin, AIChE J. **45**, 190 (1999).
[8]J. S. Kim and D. H. Reneker, Polym. Compos. **20**, 124 (1999).
[9]M. M. Bergshoef and G. J. Vancso, Adv. Mater. (Weinheim, Ger.) **11**, 1362 (1999).
[10]D. Smith and D. H. Reneker, pCT Int. Appl. (2001), Application: WO 2000-2000US27769 20001006. Priority: US 99-158673 19991008; US 2000-571444 20000516.
[11]W. Liu, M. Graham, E. A. Evans, and D. H. Reneker, J. Mater. Res. **17**, 3206 (2002).
[12]G. Zhang, Ph.D. thesis, The University of Akron, 2004.
[13]A. Buldum, C. B. Clemons, L. H. Dill, K. L. Kreider, G. W. Young, X. Zheng, E. A. Evans, G. Zhang, and S. I. Hariharan, J. Appl. Phys. **98**, 044304 (2005).
[14]U. Hansen, S. Rodgers, and K. Jensen, Phys. Rev. B **62**, 2869 (2000).
[15]V. Sukharev, Vacuum **65**, 281 (2002).
[16]P. Vogel, U. Hansen, and V. Fiorentini, Comput. Mater. Sci. **24**, 58 (2002).
[17]H. Wadley, X. Zhou, R. Johnson, and M. Neurock, Prog. Mater. Sci. **46**, 329 (2001).
[18]Y. A. Bystrov, V. L. Laska, V. A. Volpyas, E. A. Govako, D. E. Timofeev, and V. V. Troshkov, Tech. Phys. Lett. **28**, 173 (2002).
[19]S. Desa *et al.*, J. Vac. Sci. Technol. A **17**, 1926 (1999).
[20]O. Yamazaki, K. Iyanagi, S. Takagi, and K. Nanbu, Jpn. J. Appl. Phys., Part 1 **41**, 1230 (2002).
[21]N. P. Poluektov, V. N. Kharchenko, and I. G. Usatov, Plasma Phys. Rep. **27**, 625 (2001).
[22]A. Bogaerts and R. Gijbels, Vacuum **69**, 37 (2003).
[23]M. A. Lieberman and A. J. Lichtenberg, *Principles of Plasma Discharges and Materials Processing* (Wiley, New York, 1994).
[24]D. J. Economou, D. R. Evans, and R. C. Alkire, J. Electrochem. Soc. **135**, 756 (1988).
[25]M. Gegick and G. W. Young, SIAM J. Appl. Math. **54**, 877 (1994).
[26]M. P. Allen and D. J. Tildesley, *Computer Simulation of Liquids* (Oxford University Press, Oxford, 1996).
[27]A. Zhou and H. N. G. Wadley, Surf. Sci. **431**, 42 (1999).
[28]U. Hansen, P. Vogl, and V. Fiorentini, Phys. Rev. B **59**, R7856 (1999).
[29]D. E. Hanson, A. F. Voter, and J. D. Kress, J. Appl. Phys. **82**, 3552 (1997).
[30]D. G. Coronell, D. E. Hanson, A. F. Voter, C. L. Liu, and J. D. Kress, Appl. Phys. Lett. **73**, 3860 (1998).
[31]U. Hansen, S. Rodgers, and K. F. Jensen, Phys. Rev. B **62**, 2869 (2000).
[32]F. Ercolessi and J. B. Adams, Europhys. Lett. **26**, 583 (1994).
[33]A. Kersch and U. Hansen, J. Vac. Sci. Technol. A **20**, 1284 (2002).
[34]U. Hansen and A. Kersch, Phys. Rev. B **60**, 14417 (1999).

Journal of Applied Physics is copyrighted by the American Institute of Physics (AIP). Redistribution of journal material is subject to the AIP online journal license and/or AIP copyright. For more information, see http://ojps.aip.org/japo/japcr/jsp